

Article

Synthesis and Electrochemical Characterization of Dissymmetric Tetrathiafulvalene Derivatives for Aqueous Rechargeable Batteries

João F. G. Rodrigues ^{1,2}, Isabel C. Santos ¹ , Sandra Rabaça ¹  and Diogo M. F. Santos ^{2,*} 

¹ Centro de Ciências e Tecnologias Nucleares (C²TN), Instituto Superior Técnico, Universidade de Lisboa, 2695-066 Bobadela, Portugal; joao.p.faria.goncalves.rodrigues@tecnico.ulisboa.pt (J.F.G.R.); icsantos@ctn.tecnico.ulisboa.pt (I.C.S.); sandrar@ctn.tecnico.ulisboa.pt (S.R.)

² Center of Physics and Engineering of Advanced Materials, Laboratory for Physics of Materials and Emerging Technologies, Chemical Engineering Department, Instituto Superior Técnico, Universidade de Lisboa, 1049-001 Lisbon, Portugal

* Correspondence: diogsantos@tecnico.ulisboa.pt

Abstract: Organic electroactive materials (OEMs) offer advantages such as cost-effectiveness, environmental sustainability, and simplified end-of-life processing compared to inorganic electrode materials. Aqueous electrolytes further enhance sustainability and safety relative to organic electrolytes. Investigating the electrochemical properties of OEMs in aqueous media provides valuable insights into their redox behavior and stability under such conditions. However, challenges remain, including low electronic conductivity and structural stability concerns, while aqueous rechargeable batteries (ARBs) face inherent energy density limitations. Tetrathiafulvalene (TTF) has been previously reported as an electrode material for ARBs, while its oligomers have been proposed for organic electrolyte batteries. This study focuses on the synthesis and characterization of two new dissymmetric TTF derivatives—cyanobenzene tetrathiafulvalene pyrazine (CNB-TTF-Pz) (**1**) and 4-cyanobenzene tetrathiafulvalene pyrazine (4-CNB-TTF) (**2**)—as well as one symmetric TTF derivative, dipyrazine tetrathiafulvalene ((Pz)₂-TTF) (**3**). Their electrochemical behavior in aqueous lithium and potassium nitrate electrolytes was systematically characterized using cyclic voltammetry. The study provides insights into the redox properties and electroactivity of these compounds, highlighting challenges related to low electronic conductivity and redox potentials close to the water stability limits. These findings contribute to broadening our understanding of the electrochemical properties of TTF derivatives in aqueous electrolytes and offer a preliminary assessment of their potential application as electrodes for ARBs.

Keywords: tetrathiafulvalene; organic electroactive materials; organic synthesis; aqueous electrolyte; aqueous battery



Academic Editor: Junnan Hao

Received: 10 July 2024

Revised: 20 February 2025

Accepted: 25 February 2025

Published: 27 February 2025

Citation: Rodrigues, J.F.G.; Santos,

I.C.; Rabaça, S.; Santos, D.M.F.

Synthesis and Electrochemical Characterization of Dissymmetric Tetrathiafulvalene Derivatives for Aqueous Rechargeable Batteries.

Batteries **2025**, *11*, 92. <https://doi.org/10.3390/batteries11030092>

Copyright: © 2025 by the authors. Licensee MDPI, Basel, Switzerland. This article is an open access article distributed under the terms and conditions of the Creative Commons Attribution (CC BY) license (<https://creativecommons.org/licenses/by/4.0/>).

1. Introduction

Due to the push for carbon emission reduction, which has increased interest in electrical vehicles (EVs) and renewable energies, as well as the growth of consumer electronics, electrical energy storage continues to receive increasing attention as a research topic. Lithium-ion batteries (LIBs) are the most common battery chemistry used commercially for EVs and consumer electronics. However, they have several drawbacks, such as their high cost due to using rare and expensive metals (lithium and cobalt), their environmental unfriendliness, and some safety issues due to the organic electrolyte used being toxic and

flammable [1,2]. The environmental unfriendliness of LIBs stems from the toxicity of some of the metals used in them, which accumulate in the environment, wasting rare metals, as LIBs are not widely recycled due to the difficulty of the process and lack of legislation requiring their recycling [3]. Additionally, LIB fires release toxic gases, such as hydrogen fluoride and phosphoryl fluoride [2].

Organic electroactive materials (OEMs) could replace inorganic LIB electrodes, counteracting some of the drawbacks of LIBs, as they are cheaper and can be burned at the end of a battery's life cycle, allowing for some energy recovery, even if the materials are not mechanically recycled. OEMs are also more adaptable to different battery chemistries than inorganic electrodes. This means that while an inorganic electrode with suitable properties for use in LIBs is unlikely to be able to be transferable to sodium-ion, potassium-ion, or zinc-ion batteries, among others, due to differences in ionic radius and charge (in the case of zinc) negatively impacting the intercalation mechanism fundamental to LIBs, an organic electrode with suitable properties for use in LIBs is more likely to be transferable directly to other battery chemistries [3,4].

OEMs can be classified as n-type or p-type, based on whether they act as electron acceptors or electron donors. Notably, p-type OEMs donate electrons with intercalating anions [3], as opposed to the more common cation intercalation in commercial LIB cathodes and anodes. This anion intercalation means that p-type OEMs are adaptable to most battery chemistries being researched (LIBs, sodium-ion batteries, potassium-ion batteries, and multivalent-ion batteries), as the main distinguishing feature between them, the cation, is not relevant to these materials [3,4]. Furthermore, while it might be assumed that due to their nature as electron donors, these compounds would act as anodes, many p-type OEMs' reaction potential is too high for use as anodes, which leads to their use as cathodes instead. A dual-ion battery can be constructed by combining an anion-intercalating cathode and a cation-intercalating anode. These dual-ion batteries function based on an "accordion-like" mechanism, with the simultaneous deintercalation of anions and cations at the cathode and anode, respectively, during discharge, and intercalation during charge. This is in opposition to the typical cation "rocking chair" mechanism of LIBs, where cations deintercalate from the anode and intercalate into the cathode during discharge, undergoing the reverse process during charging. Nevertheless, finding p-type OEMs capable of being used as anodes would enable fully organic "anion rocking chair" batteries [3]. Low cycle life and low energy density are the most common problems preventing OEMs from being commercially used. These parameters are further lowered when conductive carbon is added to compensate for the low electrical conductivity of most OEMs. Tetrathiafulvalene (TTF), shown in Figure 1, is an example of a p-type OEM.

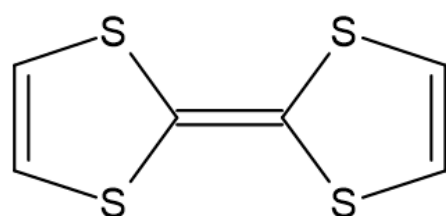
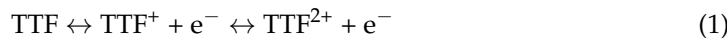


Figure 1. Molecular structure of the tetrathiafulvalene (TTF) molecule.

TTF can donate two electrons (Equation (1)) and has been studied for various applications, such as photovoltaics, organic superconductors, magnetic compounds, molecular switches [5] in molecular electronics [6], electrocatalyst for OER [7], and as a conductor and electrolyte additive in LIBs to mediate the formation of undesired species [8,9]. However, due to TTF's high solubility in organic solvents, its direct use as a cathode material in LIBs is not generally possible.



In 2019, Kato et al. [10] tested TTF extended with two benzoquinone units (one on each side) as a cathode for LIBs, SIBs, and KIBs, as well as with an ionic liquid electrolyte containing potassium ions. The addition of benzoquinone, also an electroactive molecule, increased TTF's capacity, while TTF increased benzoquinone's discharge voltage. The different cations caused the first discharge voltages to vary, achieving values of 25, 219, and 97 mAh g^{-1} for electrolytes containing Li^+ , Na^+ , and K^+ , respectively. In the second cycle, these discharge voltages increased to 236, 232, and 139 mAh g^{-1} for Li^+ , Na^+ , and K^+ , respectively. After this, the capacity quickly dropped, reaching 20% of the second cycle values by the tenth cycle. Although cyclability must be improved, these results showed TTF's ability to be used in different battery chemistries.

In the following year, Misaki et al. [11] studied derivatives of TTF with two TTF units fused with benzoquinone or naphthoquinone as cathode materials. These fused TTF molecules successfully reduced solubility, allowing for the use of TTF in organic electrolytes. The fusion of TTF with benzoquinone or naphthoquinone also increased conductivity. The compound composed of two TTF units and one benzoquinone unit showed the highest discharge capacity when tested in a LIB (299 mAh g^{-1} , 71% capacity retention after 25 cycles). The effect of conductive additives was also analyzed, and it was found that higher conductivities allowed the material to reach capacities closer to their theoretical values (when calculated per gram of active material) while also increasing capacity retention. This highlights the importance of finding ways to increase the intrinsic conductivity of OEMs, as, while conductive additive increases capacity per gram of active material, it decreases the capacity per gram of the electrode, preventing these materials from being competitive with current commercialized cathodes.

An alternative to synthesizing TTF oligomers to allow the molecule to be used in organic electrolytes is to directly use TTF as a cathode material in aqueous batteries, as the compound is insoluble in water. Aqueous electrolyte batteries have several advantages over organic electrolyte batteries, such as lower costs, non-flammability, and high rate capabilities (leading to high power density) due to water having high ionic conductivity. However, aqueous electrolytes are limited, in terms of energy density, by water's narrow electrochemical stability window (ESW). Additionally, many inorganic electrode materials are much more soluble in water than in organic electrolytes, reducing cyclability [1,12].

In 2020, Fujihara et al. [13] studied a molecular crystal couple (MCC) cathode of TTF-tetracyanoquinodimethane (TTF-TCNQ) in a 1 M NaBr aqueous electrolyte [13]. The purpose of this MCC is to allow the cathode to maintain high electrical conductivity at all states of charge through an "electrical conductivity relay" as follows: when close to full charge, there is the formation of TTF salts, which are conductive; when fully discharged, there is the formation of semiconductive TCNQ salts; and at intermediate states, the charge transfer phenomena at the TTF-TCNQ (electron donor and acceptor, respectively) results in high electrical conductivity. This electrical conductivity relay allowed the MCC cathode to reach a capacity of 112 mA h g^{-1} of active material (i.e., 104 mA h g^{-1} of the cathode, accounting for the binder) without the need for carbon additives to increase conductivity, as is common with many OEMs.

In 2023, Wang et al. [14] used TTF as a cathode for aqueous zinc-ion batteries (AZIBs), taking advantage of TTF's nature as an anion intercalating cathode to circumvent the problems associated with zinc's high ionic radius and charge. The electrolyte used was 3 M ZnCl₂ with 1 wt.% PEG700 (added to allow low-temperature testing). Notably, the results from Wang et al. suggested the possibility of TTF donating three electrons, which was supported by Gibbs free energy calculations [14]. If this possibility could be further analyzed and other systems where TTF can donate three electrons were found, TTF's theoretical capacity would increase by 50%. In Wang et al. [14], the initial capacity of the TTF cathode, at 25 °C, is 225 mA h g⁻¹ of the active material (135 mA h g⁻¹ of the cathode, accounting for the binder and conductive carbon weight).

This work focuses on the synthesis of two new dissymmetric cyanobenzene TTF derivatives, their characterization, and the investigation of their electrochemical behavior using cyclic voltammetry (CV) to provide a preliminary assessment of their suitability as electrode materials for aqueous rechargeable batteries. Their electrochemical behavior is also compared with that of a symmetric TTF derivative.

2. Materials and Methods

2.1. Synthesis

Unless purification is indicated, reagents were used as purchased. The oxo-compound (Figure 2A) and the thiones (Figure 2B,C) were synthesized following previously published procedures [15,16].

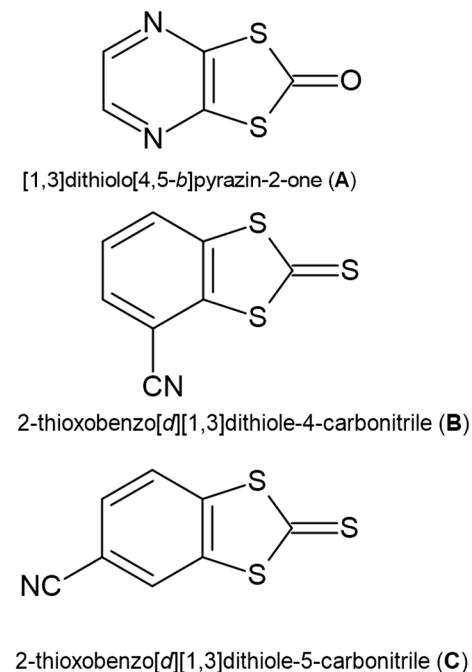


Figure 2. The molecular structures of the ketone (A) and thiones (B,C) used to synthesize the TTF derivatives.

The dissymmetric benzocyno TTF derivatives **1** and **2** (Figure 3) were obtained following a previously reported route [17,18], involving the coupling of thiones and oxo compounds in a 1:1.1 ratio, using P(OMe)₃ as a solvent for 3 h at 80 °C (Figure 3).

Afterward, the solution was vacuum-filtered and washed with cold methanol before the residue was recovered and dried. Each of the three possible reaction products was isolated through column chromatography, with the eluent being chosen by using thin-layer chromatography to determine the best option, although in cases where one product

is highly insoluble in available solvents, hot filtration should be used to isolate it. The symmetric TTF derivative (**3**) was obtained as the homo-coupling product of the reactions. Figure 4 shows a schematic representation of the reactions carried out in this work.

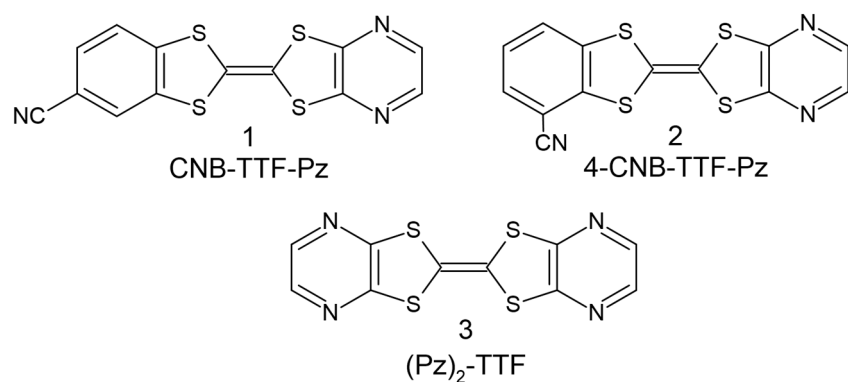


Figure 3. Designations and molecular structures of the studied compounds. (1) cyanobenzene tetrathiafulvalene pyrazine (CNB-TTF-Pz); (2) 4-cyanobenzene tetrathiafulvalene pyrazine (4-CNBTTF-Pz); and (3) dipyrazine tetrathiafulvalene ($(\text{Pz})_2\text{-TTF}$).

Thione synthesis

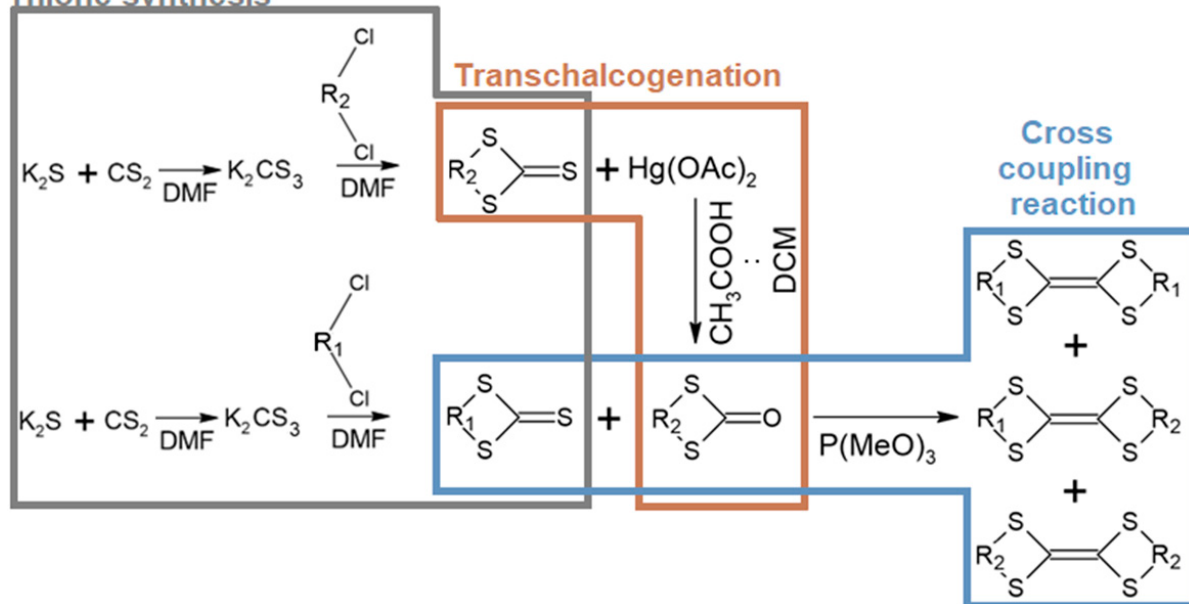


Figure 4. Schematic representation of the reaction steps involved in the synthesis of compounds **1–3** (thione synthesis and transchalcogenation carried out according to reported procedures [15,16]).

2.2. FTIR Spectrometry

FTIR spectra were obtained by analyzing the powder samples in a Thermo Scientific Nicolet iS50 (Waltham, MA, USA). Figure S1 in Supplementary Materials shows each compound's FTIR spectra.

2.3. UV–Vis Spectrometry

UV–Vis spectra were obtained by dissolving the samples in dimethyl sulfoxide and analyzing them in a Shimadzu UV-1800 (Kyoto, Japan). The UV–Vis spectra of each compound are shown in Figure S2 in Supplementary Materials.

2.4. Mass Spectrometry

Mass spectra were obtained by dissolving the samples in dichloromethane (DCM): methanol (1:5 vol.) solution and analyzing them in a Bruker Qq-TOF ImpactII (Billerica, MA, USA).

2.5. Elemental Analysis

Elemental analysis was carried out through combustion with helium as the carrier gas in a Velp EMA 502 (Usmate, Italy).

2.6. X-Ray Crystallography

Yellow single crystals of compound **2** suitable for X-ray diffraction analysis were mounted on a cryoloop with FOMBLIN protective oil. Data were acquired using a Bruker D8 QUEST diffractometer at room temperature, employing graphite-monochromated Mo K α radiation ($\lambda = 0.71073 \text{ \AA}$) in φ and ω scanning modes, and monitored through the Bruker Apex3, Crystallography Software Suite (Bruker Axs Inc., Madison, WI, USA, 2016). Data were corrected for Lorentz polarization and absorption effects and further refined based on all observed reflections using SAINT and SADABS programs [19]. The crystal structure was solved with SHELXT [20], followed by full-matrix least-squares refinement against F^2 using SHELXL [21], both included in the WINGX-version 2018.3 software package [22]. Non-hydrogen atoms were refined anisotropically, while hydrogen atoms were placed in geometrically idealized positions and refined using a riding model relative to their parent carbon atoms. Molecular visualizations were generated with Mercury 2024.3.1 software [23]. For compound **3**, the unit cell parameters correspond to a previously reported polymorph [16].

The crystallographic data for (2) is as follows: $C_{13}H_5N_3S_4$, $M = 331.44 \text{ g mol}^{-1}$, orthorhombic, space group $Pna2_1$, $a = 13.927(6) \text{ \AA}$, $b = 3.89160(10) \text{ \AA}$, $c = 23.9636(9) \text{ \AA}$, $\alpha = \beta = \gamma = 90^\circ$, $V = 1298.86(8) \text{ \AA}^3$, $Z = 4$, calc density = 1.695 Mg m^{-3} , absorption coefficient = 0.720 mm^{-1} , $F(000) = 672$, crystal size = $0.500 \times 0.040 \times 0.030 \text{ mm}$, Theta range for data collection = 2.925 to 25.677 deg ; limiting indices = $-16 \leq h \leq 16$, $-4 \leq k \leq 4$, $-29 \leq l \leq 29$; reflections collected/unique = $33,684/2475$ [$R(\text{int}) = 0.0600$]; completeness to theta = 25.242 to 99.9% ; absorption correction = semi-empirical from equivalents; max. and min. transmission 0.979 and 0.715 ; refinement method = full-matrix least-squares on F^2 ; data/restraints/parameters = $2475/1/181$; goodness of fit on $F^2 = 1.084$; final R indices [$I > 2\sigma(I)$] $R_1 = 0.0279$; $wR_2 = 0.0596$; R indices (all data) $R_1 = 0.0334$, $wR_2 = 0.0613$; absolute structure parameter = $0.06(3)$; largest diff. peak and hole = 0.222 and -0.204 e.A^{-3} , CCDC 2420208.

2.7. Scanning Electron Microscopy

SEM imaging was obtained using a JEOL JSM 7001 F (JEOL, Ltd., Tokyo, Japan) electron microscope.

2.8. Electrochemical Characterization

Electrochemical characterization was carried out using an ALS/DY2325 bipotentiostat (BAS Inc., Tokyo, Japan). The experiments were run in a 3-electrode electrochemical cell using a glassy carbon (GC) working electrode, a saturated calomel electrode (SCE) reference electrode, and a platinum counter-electrode. The GC electrode had an area of 0.07 cm^2 , where the catalyst inks were deposited. Anodic currents were set as positive in the bipotentiostat software, and all potentials shown are vs. SCE, as that was the reference electrode used. Unless otherwise stated, all CVs shown correspond to the first cycle.

CVs were performed after deaerating the electrolyte solution for 25 min with nitrogen bubbling and then keeping the experimental setup covered with parafilm to prevent aeration during the test. All compounds were tested in 1 M LiNO₃. Compound **3** was additionally tested in 2 and 3 M LiNO₃, and compound **2** was tested in 1 M KNO₃.

The electrode inks were prepared by adding 5 mg of the compound to 125 μL of a 2 wt.% PVDF in *n*-methyl-2-pyrrolidone solution, which was sonicated for 30 min. Afterward, 5 μL of the dispersion was added to the GC electrode and dried at 50 °C overnight.

3. Results

3.1. Compound **1** Synthesis

Thione C (0.222 g; 1 mmol) and oxo-compound A (0.189 g; 1.1 mmol) were mixed with 10 mL of P(OMe)₃ and stirred for 3 h at 80 °C under inert atmosphere. After cooling, the orange precipitate was filtered, washed three times with 10 mL of cold MeOH, and dried under vacuum. The solid was purified by an initial hot filtration with DCM as the solvent, followed by column chromatography, using DCM:ethyl acetate (30:1 vol.) solution as eluent. R_f = 0.59; FTIR (cm⁻¹): ν = C-H (3063), CN (2225), C=C (1574), C-H (871), C-S (818); UV-Vis (nm): 278, 306, 391; elemental analysis for C₁₃H₅N₃S₄ (331): C 47%, H 1.5%, N 13%, S 39%; found: C 47%, H 1.6%, N 12%, S 36%.

It was possible to isolate the product of the homocoupling reaction of the ketone (compound **3** R_f = 0.10). Compound **3**, *m/z* = 308.9363; FTIR (cm⁻¹): ν = C-H (2922), C=C (1534), C-H (843), C-S (771); UV-Vis (nm): 257, 281, 302, 398.

3.2. Compound **2** Synthesis

Thione B (0.209 g; 1 mmol) and oxo-compound A (0.188 g; 1.1 mmol) were mixed with 10 mL of P(OMe)₃ and stirred for 3 h at 80 °C under inert atmosphere. After cooling, the orange precipitate was filtered, washed three times with 10 mL of cold MeOH, and dried under vacuum. The solid was purified by column chromatography, using DCM:hexane (3:2 vol.) solution as eluent (0.118 g; 0.356 mmol, yield = 59%, R_f = 0.24). *m/z* = 331.9490; FTIR (cm⁻¹): ν = C-H (3072 and 2922), CN (2227), C=C (1563), C-H (842), C-S (783); UV-Vis (nm): 255, 285, 307, 395; elemental analysis for C₁₃H₅N₃S₄ (331): C 47%, H 1.5%, N 13%, S 39%; found: C 48%, H 1.9%, N 12%, S 37%.

It was possible to isolate the product of the homocoupling reaction of the ketone (compound **3**, 0.017 g; 0.0551 mmol, yield = 8.5%, R_f = 0.11, *m/z* = 308.9363, FTIR (cm⁻¹): ν = C-H (2923), C=C (1534), C-H (842), C-S (771)).

3.3. Crystal Structure

Single crystals of compound **2** suitable for X-ray analysis were grown by slow evaporation from a dichloromethane solution. The X-ray structural refinement confirms the molecular structure of compound **2** and was found to crystallize in the orthorhombic system, space group *Pna2*₁ with one crystallographically independent molecule in a general position (Figure 5).

This molecule is almost planar with a boat conformation. The central C=C bond length (C9-C8 = 1.335(5) Å) is typical of neutral TTF donors [24].

The crystal structure is formed by stacking molecules head-to-head, forming stacks along the *b* axis (Figure 6) with short S···S contacts (S2···S3) and short C-H···C≡N (C13-H13···N1≡C7) and C-H···N (C5-H5···N3). Short-contact details are given in Table 1. Molecules in neighboring stacks along *a* are tilted by 78.71°.

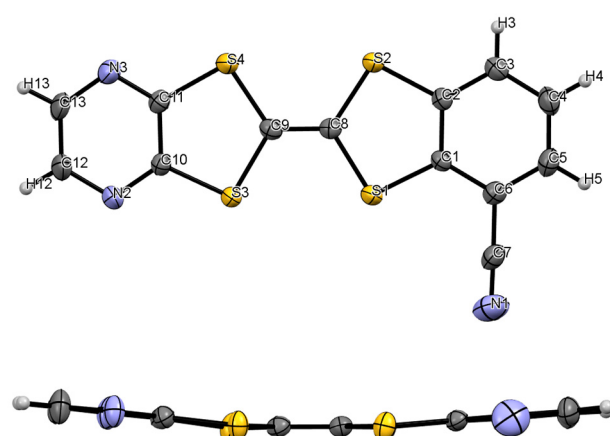


Figure 5. ORTEP diagrams of compound **2** drawn at a 50% probability level with the atomic numbering scheme, top and lateral view.

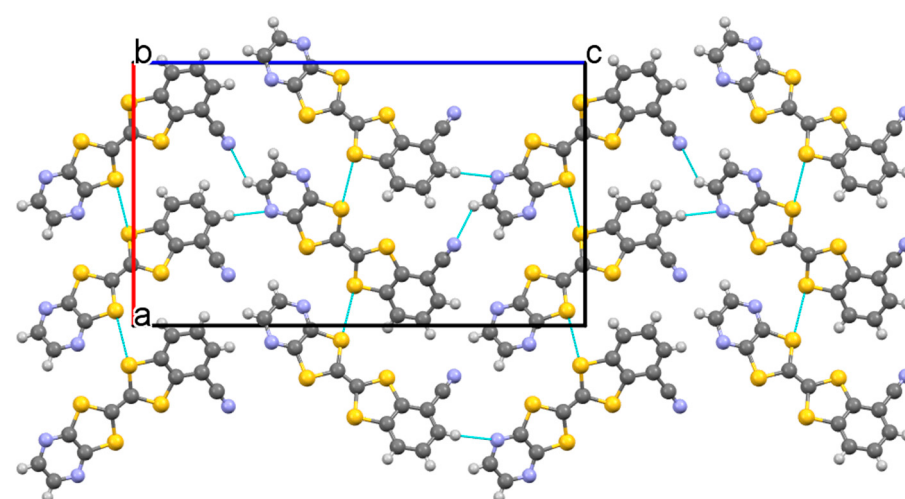


Figure 6. Crystal structure of **2**, view along the *b*-axis. Short contacts are represented in light blue.

Table 1. C-H···N≡C, C-H···N, and S···S short contacts in **2**.

| Short Contact | Symmetry Operation | Length (Å) | Length- $\sum VdW$ (Å) |
|------------------|----------------------------|------------|------------------------|
| C13-H13···N1≡C71 | 1 - x, 1 - y, -1/2 + z | 2.599 | -0.151 |
| C5-H5···N3 | 1.5 - x, -1/2 + y, 1/2 + z | 2.660 | -0.090 |
| S3···S2 | -1/2 + x, 1/2 - y, z | 3.375 (2) | -0.225 |
| N2···S2 | -1/2 + x, 1/2 - y, z | 3.414 (4) | 0.006 |
| N2···S4 | -1/2 + x, 1/2 - y, z | 3.541 (4) | 0.191 |

3.4. SEM Imaging

Figure 7 shows the SEM images obtained for all compounds at two different resolutions. As can be seen, compound **1** forms amorphous plates, while compound **2** forms rectangular or square plates (Figure 7a,c). These plates are made up of smaller needle-like crystals in the case of compound **1** (Figure 7b), while in the case of compound **2**, the plates are covered by needle-like crystals (Figure 7d). In the case of compound **3**, the needle-like crystals are instead arranged into columns (Figure 7e,f).

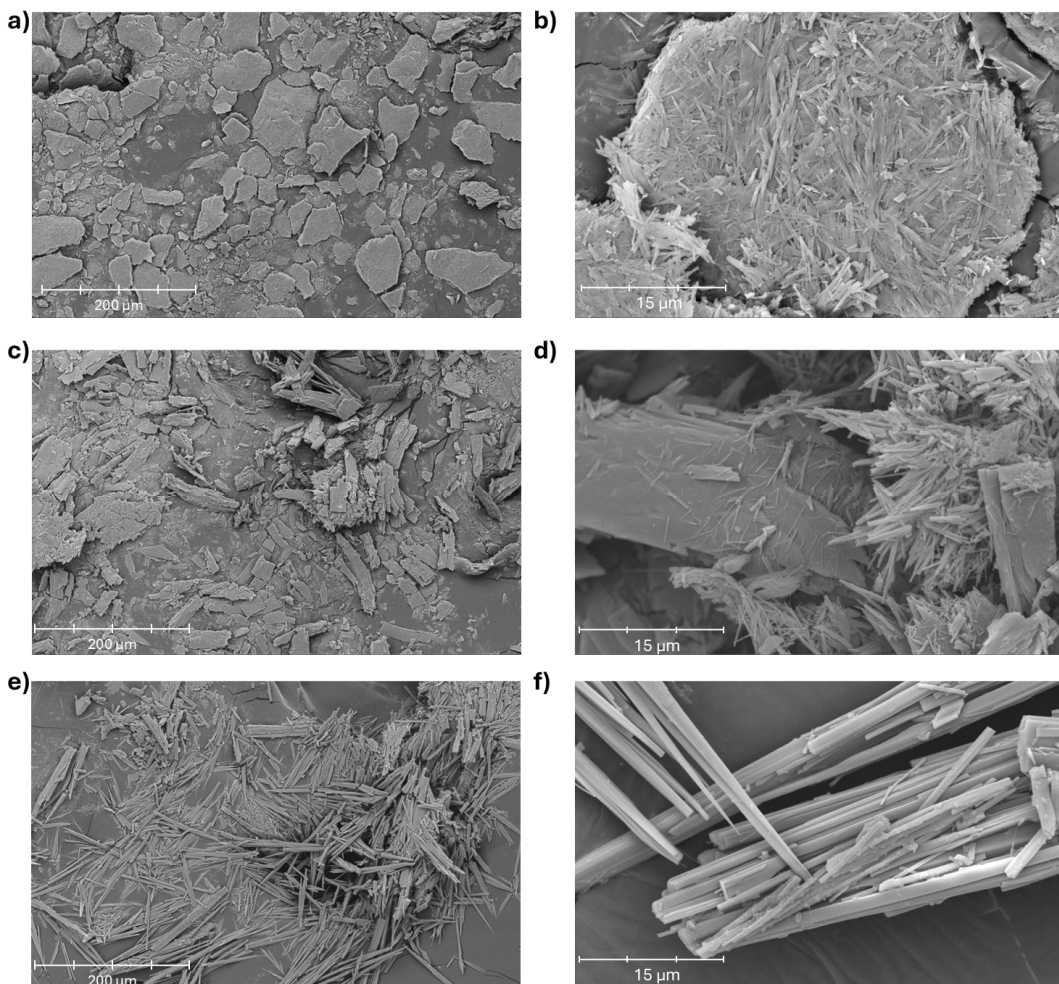


Figure 7. SEM imaging for compound **1** (**a,b**), compound **2** (**c,d**), and compound **3** (**e,f**) at $200\times$ magnification (**a,c,e**) and at $2500\times$ magnification (**b,d,f**).

3.5. Electrochemical Studies

3.5.1. Effect of Scan Rate

Firstly, the effect of increasing the scan rate was studied for the three compounds, using 1 M LiNO₃ as the electrolyte. The CVs obtained are shown in Figure 8.

Figure 8a shows the full CVs for compound **1** in 1 M LiNO₃ at different scan rates. Two cathodic peaks can be observed. The cathodic peak at higher potentials does not become broader with increasing scan rate, but the lower potential cathodic peak does. The high potential cathodic peak is paired with an anodic peak, which becomes more difficult to detect with an increase in the scan rate, and a potential anodic peak at -0.1 V can only be seen at 10 mV s^{-1} . The high potential cathodic peak shows a comparable current at 50 and 100 mV s^{-1} , suggesting that it is not dependent on the scan rate and, consequently, not diffusion controlled.

Figure 8b shows the full CVs for compound **2** in 1 M LiNO₃. Both a cathodic and anodic peak with considerable separation can be observed. The cathodic peak is centered at around -1 V when scanned at 10 mV s^{-1} , shifting to -1.25 V at 50 mV s^{-1} . The anodic peak is centered at around 0 V when scanned at 10 mV s^{-1} and shifts to 0.25 V at 50 mV s^{-1} . Aside from shifting to higher or lower potentials (for the anodic and cathodic peaks, respectively), the cathodic peak broadens considerably with an increase in the scan rate compared to the anodic peak.

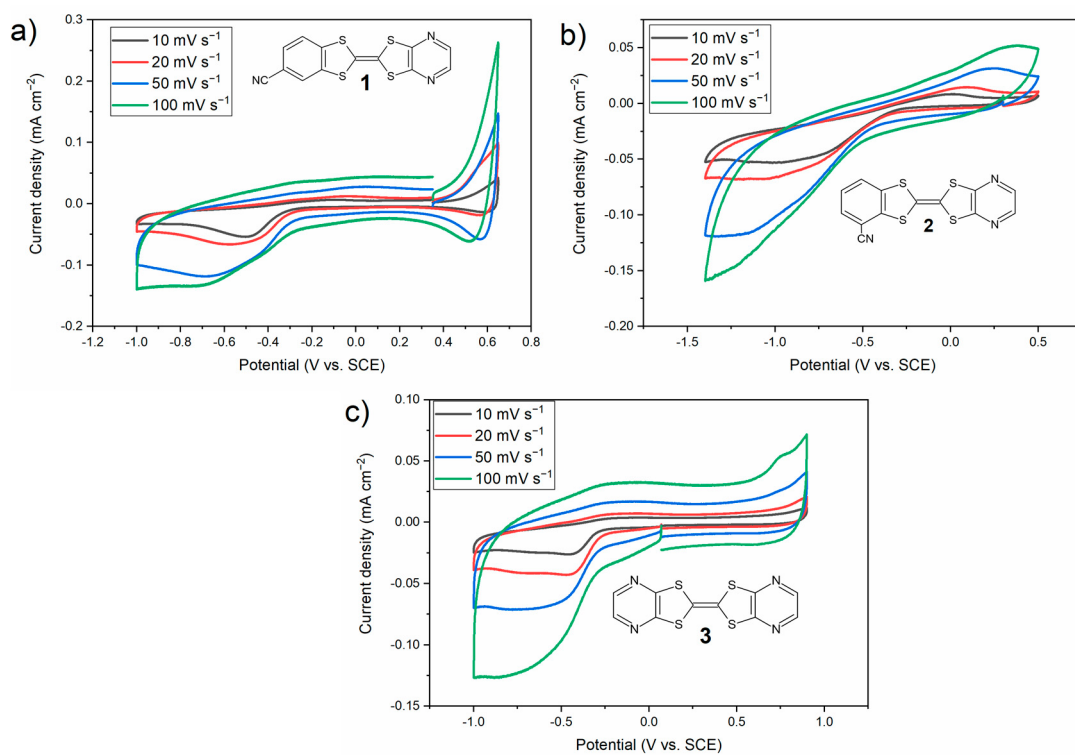


Figure 8. Effect of the scan rate on each compound in a 1 M LiNO₃ electrolyte. (a) compound 1; (b) compound 2; and (c) compound 3.

Figure 8c shows the full CVs for compound 3 in 1 M LiNO₃. A cathodic peak can be observed at around -0.5 V when the compound is scanned at 10 mV s^{-1} . This peak broadens and shifts to lower potentials with an increase in the scan rate. At 100 mV s^{-1} , the peak appears to be centered at around -1 V, but the start of HER prevents the peak from being fully observed. While no anodic peaks can be seen at 10 or 50 mV s^{-1} , at 100 mV s^{-1} , an anodic peak at 0.75 V can be seen, although this is not fully developed due to the start of OER. Once again, both peaks are considerably separated, but two bands with low current density can be seen centered at slightly below 0 V (anodic band) and 0.75 V (cathodic band), which might correspond to the pairs of the peaks observed at -1 V and 0.75 V (at a scan rate of 100 mV s^{-1}).

3.5.2. Effect of Electrolyte Concentration

The effect of electrolyte concentration on the CVs of compound 3 was studied using 1, 2, and 3 M LiNO₃ electrolyte solutions (Figure 9).

When first tested in 3 M LiNO₃, compound 3 showed a cathodic peak at ca. -1 V. The peak current density decreased to half the value in the second cycle, shifting to higher potentials under continuous cycling until settling at around -0.5 V. This indicates that compound 3 requires activation by being exposed to low potentials to allow for the formation of more electroactive species and possible structural changes.

The increase in electrolyte concentration leads to increased peak current densities, making the cathodic peak at -0.5 V more defined. The 3 M LiNO₃ electrolyte also causes two anodic peaks to become visible, one at around -0.1 V and another at around -0.8 V. The increase in current is expected due to higher concentrations leading to higher electrolyte conductivity (although this relationship is not linear).

The reaction order for each of these peaks was calculated by selecting a potential that best aligns with the center of a peak at different concentrations and a constant scan rate and by obtaining the current corresponding to that potential value (j_x , with x corresponding to

the potential that was chosen) for each concentration. The reaction order is equal to the slope of $\log(j_x)$ vs. $\log(\text{concentration})$. Table 2 shows the j_x values and the obtained reaction orders with their respective R^2 values. Note that $j_{-0.5}$ and $j_{-0.1}$ were obtained from the CVs at 10 mV s^{-1} , while $j_{0.8}$ was obtained from the CVs at 50 mV s^{-1} .

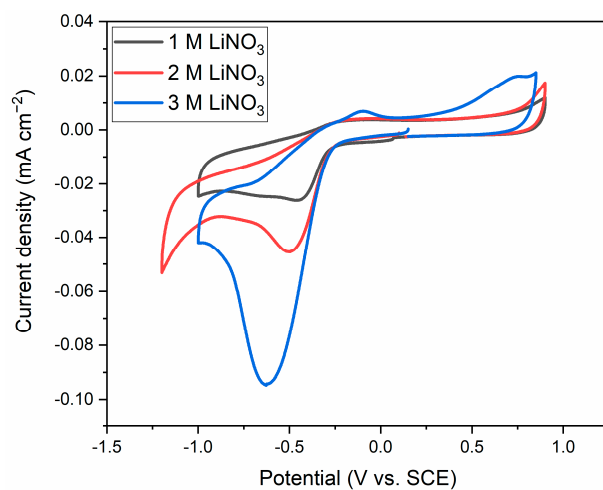


Figure 9. Effect of the LiNO_3 electrolyte concentration on the cyclic voltammograms of compound 3 at 10 mV s^{-1} .

Table 2. Calculated reaction order and recorded current densities at selected potentials for compound 3.

| LiNO_3 Conc. (M) | $j_{-0.5}$ (mA cm^{-2}) | $j_{-0.1}$ (mA cm^{-2}) | $j_{0.8}$ (mA cm^{-2}) |
|------------------------------|---------------------------------------|---------------------------------------|--------------------------------------|
| 1 | -0.026 | 0.0038 | 0.029 |
| 2 | -0.051 | 0.0043 | 0.037 |
| 3 | -0.081 | 0.0069 | 0.053 |
| Reaction order | 1.03 | 0.51 | 0.52 |
| R^2 | 0.99 | 0.79 | 0.93 |

3.5.3. Effect of the Counter-Cation

Compound 2 was additionally tested in 1 M KNO_3 to analyze the effect of the counter-cation. Figure 10 shows the CVs for compound 2 scanned at 20 mV s^{-1} in both 1 M LiNO_3 and 1 M KNO_3 .

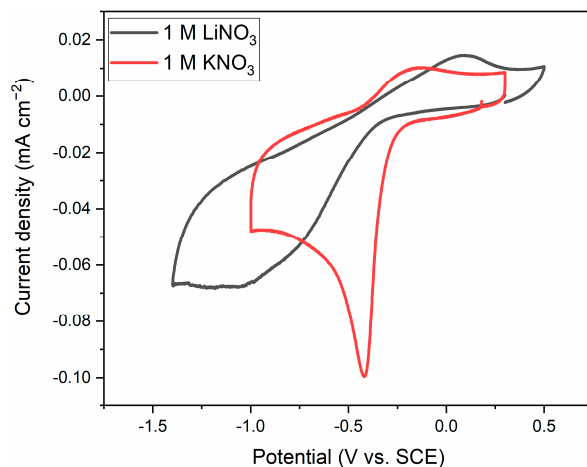


Figure 10. Effect of counter-cation on the electrochemical behavior of compound 2 at 20 mV s^{-1} .

The peaks showed much less separation in 1 M KNO₃. Additionally, while the anodic peak current was comparable in both electrolytes, the cathodic peak was much sharper in 1 M KNO₃ and showed higher currents.

4. Discussion

To understand the results of this work, it is essential to clarify that TTF is insoluble in aqueous electrolytes and soluble in organic electrolytes, leading to significant differences in its electrochemical behavior. Rather than simply oxidizing in two steps, as described in Equation (1) for organic media, TTF in aqueous electrolytes will oxidize in three steps. First, the solid TTF will partially oxidize until a solid with stoichiometry TTFX_n ($n < 1$; X = monovalent anion) is formed. In this state, some of the TTF is neutral while some is monocationic; this can be represented as $(TTF^{+•})_n(TTF)_{1-n}X_n$ to better illustrate the change. This mixed valence salt will then be further oxidized until all TTF is in the monocationic state, forming $(TTF^{+•})X$. Lastly, this solid will be oxidized until all TTF is in the dicationic state, forming $(TTF^{2+})X_2$ [13,25–27].

The reaction orders shown in Table 2 are significant, given the expected behavior of TTF. While the 0.5 values agree with the known behavior of TTF in nitrate solutions (two redox reactions intercalating 0.5 moles of nitrate each [25]), the value close to 1 contradicts this. The modifications to the TTF molecule could affect its redox behavior, causing the intercalation to occur in two steps (0.5 moles of nitrate each), while deintercalation occurs in one step (1 mole of nitrate). This indicates the possibility of compound 3 undergoing conformational changes differently from TTF during the intercalation–deintercalation process, favoring deintercalation which occurs in a single step [28,29].

The difference between the CVs obtained and the one shown by Adeel et al. [25], which was also obtained in aqueous nitrate solution, is considerable. For a concentration of 0.1 M Co(NO₃)₂, two to three (depending on the switching potential chosen) pairs of peaks can be seen, with both the cathodic and anodic peaks having comparable current values. For a 1 M Co(NO₃)₂ concentration, the peaks observed in the 0–200 mV range remained at around the same potentials. Furthermore, Adeel et al. [19] reported redox peaks located in the 0–600 mV range (vs. Ag/AgCl, with similar potential to the herein used SCE), as opposed to the compounds in this study, which exhibit peaks in a much broader range, i.e., from –1 to 1 V vs. SCE, depending on the compound.

When observing Figure 8, it may be considered that compounds **1** and **3** have two potential ranges at which they are electroactive, with an inert zone in between. These compounds exhibit peaks around 0.5 V, coinciding with the potential at which Adeel et al. observed the third pair of redox peaks [25], when the switching potential is 750 mV. Wang et al. [14] reported CVs of TTF in aqueous ZnCl₂. Once again, three pairs of peaks can be seen, with both the anodic and cathodic peaks having comparable current values. While the relative positions of the peaks are slightly different from those reported by Adeel et al. [25], it is difficult to say whether this difference can be attributed to the difference in the anion or the difference in the scan rate and temperature. In either case, the difference in the CVs of Wang et al. [14] and Adeel et al. [25] is less stark than the difference in the CVs of compound **2** in 1 M LiNO₃ and 1 M KNO₃ (Figure 9).

The exact electrochemical processes behind the CVs obtained are still unknown. However, testing the same compound in different concentrations of the same electrolyte can help better understand the observed redox processes, as shown by the experimental work carried out with compound **3**. As such, testing the compounds in various concentrations of the same salt could yield valuable information. Higher concentrations could also help minimize the HER and OER [1], making the implementation of these materials into aqueous battery chemistries feasible.

Iwamoto et al. [30] tested extended TTFs for battery applications and found that the materials showed both one- and two-electron redox processes. This was concluded to be caused by the effect of electrostatic interactions caused by the extended TTFs' molecular geometry. Several of the materials tested also exhibited two regions of electroactivity, separated by an inert region. This could indicate that the reaction orders in Table 2—suggesting that the oxidation occurs in two 0.5 electron steps while the reduction occurs in a 1 electron step—could result from not only morphological changes but also electrostatic effects in the molecule.

The better results for the 1 M KNO₃ electrolyte, when compared to the 1 M LiNO₃ electrolyte for compound 2 (Figure 10), in terms of cathodic peak sharpness and both peaks being at a potential where HER and OER are not a factor, show the potential for application of these materials in battery chemistries other than aqueous rechargeable lithium-ion batteries (ARLIBs). For all compounds, the increase in the scan rate was often associated with the broadening and shifting of cathodic peaks, but it also allowed anodic peaks to become more defined (Figure 8). The increase in electrolyte concentration also had a similar effect on peak definition (Figure 9). There was no indication of the electrode materials dissolving into the solution or becoming physically compromised when observed before and after use.

5. Conclusions

This work presents a preliminary electrochemical assessment of three synthesized TTF derivatives. The results suggest that further studies are needed to better understand the electrochemical properties and potential applications of these compounds as electrode materials for aqueous rechargeable batteries.

In general, the CVs for these compounds exhibited one well-defined cathodic peak. Anodic peaks were much broader, with significantly lower current densities, and, in some cases, more than 500 mV apart from the cathodic peak. Some compounds exhibited a second cathodic peak with a much lower current density. The differences in current density and the separation between peaks make it challenging to understand the exact redox processes underlying the CVs obtained. The known behavior of TTF in aqueous solutions allows for inferring some preliminary mechanisms for (Pz)₂-TTF (3), corroborated by the calculated reaction orders for each peak. Still, further studies are needed to fully elucidate these systems. Additionally, some compounds exhibited considerable peak shifting and broadening with an increase in the scan rate, indicating slow kinetics and some degree of irreversibility, which further impact their electrochemical performance.

The current densities were relatively low, leading to slow charge/discharge kinetics, affecting their feasibility for battery applications. While the addition of conductive carbon is known to enhance the conductivity of electrode materials, this was not carried out here to evaluate the intrinsic electrochemical behavior of the synthesized compounds without external contributions. Although adding carbon would increase conductivity, it would also reduce specific capacity and would not resolve another key challenge in aqueous battery applications as follows: several compounds exhibited redox peaks at potentials where water decomposition occurs via HER or OER. Thus, to ensure safe operation, these materials would have to operate within a limited potential window, further limiting capacity, as they would not be fully oxidized or reduced.

By comparing the results obtained for the same compound in lithium nitrate and potassium nitrate, it was observed that these materials exhibit different electrochemical behavior depending on electrolyte composition. This adaptability could contribute to more versatile and potentially more cost-effective battery chemistries. Moreover, the synthetic strategies used in this study provide a straightforward approach for obtaining different

TTF derivatives, with purification achievable through simple techniques, enabling future modifications and optimizations.

Supplementary Materials: The following supporting information can be downloaded at: <https://www.mdpi.com/article/10.3390/batteries11030092/s1>, Figure S1: FTIR spectra for (a) compound 1, (b) compound 2, and (c) compound 3.; Figure S2: UV–Vis spectra for (a) compound 1, (b) compound 2, and (c) compound 3.

Author Contributions: Conceptualization, S.R. and D.M.F.S.; methodology, J.F.G.R., S.R., D.M.F.S. and I.C.S.; investigation, J.F.G.R. and I.C.S.; writing—original draft preparation, J.F.G.R.; writing—review and editing, S.R. and D.M.F.S.; visualization, J.F.G.R. and I.C.S.; supervision, S.R. and D.M.F.S. All authors have read and agreed to the published version of the manuscript.

Funding: The authors would like to thank Fundação para a Ciência e a Tecnologia (FCT, Portugal) for funding the exploratory project PEX 2023.15074 (<https://doi.org/10.54499/2023.15074.PEX>, accessed on 20 February 2025), the research grant under project UIDP/04540/2020 (J. F. G. Rodrigues), contract 2023.09426.CECIND under the Individual Call to Scientific Employment Stimulus—6th Edition (D.M.F. Santos), contract UIDB/Multi/04349/2020 (S. Rabaça).

Data Availability Statement: The data presented in this study are available upon request from the corresponding author.

Conflicts of Interest: The authors declare no conflicts of interest.

References

1. Von Wald Cresce, A.; Xu, K. Aqueous lithium-ion batteries. *Carbon Energy* **2021**, *3*, 721–751. [[CrossRef](#)]
2. Larsson, F.; Andersson, P.; Blomqvist, P.; Mellander, B.E. Toxic fluoride gas emissions from lithium-ion battery fires. *Sci. Rep.* **2017**, *7*, 10018. [[CrossRef](#)]
3. Esser, B.; Dolhem, F.; Becuwe, M.; Poizot, P.; Vlad, A.; Brandell, D. A perspective on organic electrode materials and technologies for next generation batteries. *J. Power Sources* **2021**, *482*, 228814. [[CrossRef](#)]
4. Shea, J.J.; Luo, C. Organic Electrode Materials for Metal Ion Batteries. *ACS Appl. Mater. Interfaces* **2020**, *12*, 5361–5380. [[CrossRef](#)] [[PubMed](#)]
5. Canevet, D.; Sallé, M.; Zhang, G.; Zhang, D.; Zhu, D. Tetrathiafulvalene (TTF) derivatives: Key building-blocks for switchable processes. *Chem. Commun.* **2009**, *17*, 2245–2269. [[CrossRef](#)] [[PubMed](#)]
6. Ward, J.S.; Vezzoli, A. Key advances in electrochemically-addressable single-molecule electronics. *Curr. Opin. Electrochem.* **2022**, *35*, 101083. [[CrossRef](#)]
7. Xia, W.; Ji, C.; Wang, R.; Qiu, S.; Fang, Q. Metal-Free Tetrathiafulvalene Based Covalent Organic Framework for Efficient Oxygen Evolution Reaction. *Wuli Huaxue Xuebao Acta Phys. Chim. Sin.* **2023**, *39*, 2212057. [[CrossRef](#)]
8. Torres, W.R.; Herrera, S.E.; Tesio, A.Y.; Del Pozo, M.; Calvo, E.J. Soluble TTF catalyst for the oxidation of cathode products in Li-Oxygen battery: A chemical scavenger. *Electrochim. Acta* **2015**, *182*, 1118–1123. [[CrossRef](#)]
9. Zhang, J.; Sun, B.; Zhao, Y.; Kretschmer, K.; Wang, G. Modified Tetrathiafulvalene as an Organic Conductor for Improving Performances of Li–O₂ Batteries. *Angew. Chem.* **2017**, *129*, 8625–8629. [[CrossRef](#)]
10. Kato, M.; Masese, T.; Yao, M.; Takeichi, N.I.; Kiyobayashi, T. Organic positive-electrode material utilizing both an anion and cation: A benzoquinone-tetrathiafulvalene triad molecule, Q-TTF-Q, for rechargeable Li, Na, and K batteries. *New J. Chem.* **2019**, *43*, 1626–1631. [[CrossRef](#)]
11. Misaki, Y.; Noda, S.; Kato, M.; Yamauchi, T.; Oshima, T.; Yoshimura, A.; Shirahata, T.; Yao, M. Fused Tetrathiafulvalene and Benzoquinone Triads: Organic Positive-Electrode Materials Based on a Dual Redox System. *ChemSusChem* **2020**, *13*, 2312–2320. [[CrossRef](#)] [[PubMed](#)]
12. Chen, S.; Jeong, S.R.; Tao, S. Key materials and future perspective for aqueous rechargeable lithium-ion batteries. *Mater. Rep. Energy* **2022**, *2*, 100096. [[CrossRef](#)]
13. Fujihara, Y.; Kobayashi, H.; Takaishi, S.; Tomai, T.; Yamashita, M.; Honma, I. Electrical Conductivity-Relay between Organic Charge-Transfer and Radical Salts toward Conductive Additive-Free Rechargeable Battery. *ACS Appl. Mater. Interfaces* **2020**, *12*, 25748–25755. [[CrossRef](#)] [[PubMed](#)]
14. Wang, J.; Zhang, X.; Yan, Z.; Rui, Z.; Yang, Z.; Huang, Y.; Deng, W. Tetrathiafulvalene as a sustainable cathode with high rate and Long Life-span for aqueous Zinc-ion battery at low temperatures. *Chem. Eng. J.* **2023**, *459*, 141649. [[CrossRef](#)]

15. Cerdeira, A.C.; Afonso, M.; Santos, I.; Pereira, L.; Coutinho, J.; Rabaça, S.; Simão, D.; Henriques, R.; Almeida, M. Synthesis, structure and physical properties of transition metal bis 4-cyanobenzene-1,2-dithiolate complexes $[M(cbdt)2]z^-$ ($M = Zn, Co, Cu, Au, Ni, Pd$, $z = 0, 1, 2$). *Polyhedron* **2012**, *44*, 228–237. [[CrossRef](#)]
16. Rabaça, S.; Oliveira, S.; Santos, I.C.; Almeida, M. Extended TTF-type donors fused with pyrazine units; synthesis and characterization. *Tetrahedron Lett.* **2013**, *54*, 6635–6639. [[CrossRef](#)]
17. Fabre, J.M.; Giral, L.; Dupart, E.; Coulon, C.; Manceau, J.P.; Delhaès, P. Organic metals. A new series of radical-cation salts based on an unsymmetrically alkylated tetraselenafulvalene molecule. *J. Chem. Soc.* **1983**, *24*, 1477–1479. [[CrossRef](#)]
18. Fabre, J.M. Synthesis strategies and chemistry of nonsymmetrically substituted tetrachalcogenafulvalenes. *Chem. Rev.* **2004**, *104*, 5133–5150. [[CrossRef](#)]
19. Bruker Analytical Systems. *Reference Manuals, Bruker AXS:SAINT+, Release 6.22. and Bruker AXS:SADABS*; Bruker Analytical Systems: Madison, WI, USA, 2005.
20. Sheldrick, G.M. *SHELXT—Integrated space-group and crystal-structure determination*. *Acta Crystallogr. Sect. A Found. Adv.* **2015**, *71*, 3–8. [[CrossRef](#)] [[PubMed](#)]
21. Sheldrick, G.M. Crystal structure refinement with *SHELXL*. *Acta Crystallogr. Sect. C Struct. Chem.* **2015**, *71*, 3–8. [[CrossRef](#)] [[PubMed](#)]
22. Farrugia, L. WinGX and ORTEP for Windows: An update. *J. Appl. Crystallogr.* **2012**, *45*, 849–854. [[CrossRef](#)]
23. Macrae, C.F.; Sovago, I.; Cottrell, S.J.; Galek, P.T.A.; McCabe, P.; Pidcock, E.; Platings, M.; Shields, G.P.; Stevens, J.S.; Towler, M.; et al. *Mercury 4.0: From visualization to analysis, design and prediction*. *J. Appl. Crystallogr.* **2020**, *53*, 226–235. [[CrossRef](#)] [[PubMed](#)]
24. Varatojo, A.; Lopes, G.; Gama, V.; Oliveira, G.; Santos, I.C.; Lopes, E.B.; Simão, D.; Almeida, M.; Rabaça, S. Bromide and Tribromide 4-Cyanobenzene-Ethylenedithio-Tetrathiafulvalene Radical Salts by Chemical and Electrochemical Routes. *Cryst. Growth Des.* **2019**, *19*, 5768–5775. [[CrossRef](#)]
25. Adeel, S.M.; Martin, L.L.; Bond, A.M. Redox-induced solid-solid state transformation of tetrathiafulvalene (TTF) microcrystals into mixed-valence and π -dimers in the presence of nitrate anions. *J. Solid State Electrochem.* **2014**, *18*, 3287–3298. [[CrossRef](#)]
26. Gómez, L.; Rodríguez-Amaro, R. Nucleation and growth of thin films of the organic conductor TTF-iodide over glassy carbon. Electrochemical and spectroelectrochemical study. *Langmuir* **2009**, *25*, 4799–4803. [[CrossRef](#)] [[PubMed](#)]
27. Scott, B.A.; Placa, S.J.L.; Torrance, J.B.; Silverman, B.D.; Welber, B. The crystal chemistry of organic metals. composition, structure, and stability in the tetrathiafulvalinium-halide systems. *J. Am. Chem. Soc.* **1977**, *99*, 6631–6639. [[CrossRef](#)]
28. Elgrishi, N.; Rountree, K.J.; McCarthy, B.D.; Rountree, E.S.; Eisenhart, T.T.; Dempsey, J.L. A Practical Beginner’s Guide to Cyclic Voltammetry. *J. Chem. Educ.* **2018**, *95*, 197–206. [[CrossRef](#)]
29. Bard, A.J.; Faulkner, L.R. *Electrochemical Methods: Fundamentals and Applications*, 2nd ed.; John Wiley & Sons: Hoboken, NJ, USA, 2001; p. 475.
30. Iwamoto, S.; Inatomi, Y.; Ogi, D.; Shibayama, S.; Murakami, Y.; Kato, M.; Takahashi, K.; Tanaka, K.; Hojo, N.; Misaki, Y. New tris- and pentakis-fused donors containing extended tetrathiafulvalenes: New positive electrode materials for rechargeable batteries. *Beilstein J. Org. Chem.* **2015**, *11*, 1136–1147. [[CrossRef](#)]

Disclaimer/Publisher’s Note: The statements, opinions and data contained in all publications are solely those of the individual author(s) and contributor(s) and not of MDPI and/or the editor(s). MDPI and/or the editor(s) disclaim responsibility for any injury to people or property resulting from any ideas, methods, instructions or products referred to in the content.